



Amorphous CoFeB nanosheets with plasmon-regulated dynamic active sites for electrocatalytic water oxidation



Huayu Chen^a, Junxiang Chen^b, He He^a, Xin Chen^c, Chunguang Jia^{b,d}, Da Chen^{a,*}, Junhui Liang^a, Dandan Yu^a, Xin Yao^e, Laishun Qin^{a,*}, Yuexiang Huang^a, Zhenhai Wen^{b,*}

^a College of Materials and Chemistry, China Jiliang University, Hangzhou 310018, China

^b CAS Key Laboratory of Design and Assembly of Functional Nanostructures, Fujian Provincial Key Laboratory of Nanomaterials, Fujian Institute of Research on the Structure of Matter, Chinese Academy of Sciences, Fuzhou 350002, China

^c TJU-NIMS International Collaboration Laboratory, School of Material Science and Engineering, Tianjin University, Tianjin 300072, China

^d Key Laboratory of Jiangxi Province for Persistent Pollutants Control and Resources Recycle, Nanchang Hangkong University, Nanchang 330063, China

^e College of Optical and Electronic Technology, China Jiliang University, Hangzhou 310018, China

ARTICLE INFO

Keywords:

Surface plasmon resonance
Surface reconstruction
Active sites
Water oxidation
Metal boride

ABSTRACT

Exploring efficient and low-cost oxygen evolution reaction (OER) electrocatalysts is of crucial importance. Here, we report a surface plasmon resonance (SPR) engineering strategy to regulate surface reconstruction of CoFeB nanosheets by decorating plasmonic MoO₂ nanospheres (MoO₂/CoFeB), in which the SPR effect of MoO₂ offers an additional acceleration for the conversion of inactive Co species to active cobalt oxyhydroxide on the CoFeB surface under visible light. Our results also indicate the real reactive surface for CoFeB is in the form of CoFeOOH with adsorbed BO₂⁻ that has positive effect. The MoO₂/CoFeB shows superior OER performance with a low overpotential (209 mV at $J=10 \text{ mA cm}^{-2}$). However, such an accelerated reconstruction behavior would be self-terminated once the anodic voltage increases to thoroughly oxidize the MoO₂ to high valence state (+6). This work inspires us to develop a rational strategy to improve the catalytic performance by properly regulating the surface reconstruction.

1. Introduction

With the common goal of carbon neutrality worldwide, the development of hydrogen energy with synergy of the burgeoning renewable electricity (e.g., windy, solar) is envisaged as an effective and sustainable approach to reduce carbon emissions [1,2]. The sluggish kinetics of the oxygen evolution reaction (OER) is one of the most serious bottlenecks that limit the efficiency of electrolytic hydrogen production [3,4]. Recently, the first-row 3d transition metals (TM) and their compounds (e.g., chalcogenide, nitride, phosphide and boride) have been reported to undergo a dynamic surface-reconstruction process in alkaline electrolyte [5–7]. The real active sites for these catalysts are *in situ* produced amorphous or low crystalline oxyhydroxide (TMOOH) intermediates [8, 9]. Among the TM-based catalysts, amorphous metal borides are attractive due to their low energy barrier of the hydroxylation reaction and abundant active sites [10], it is thus highly desirable to develop regulatable strategies to implement the surface reconstruction of metal borides for boosting the associated electrocatalytic activity.

External fields have been widely applied to intensify the electrochemical reaction [11], which can be feasibly used for surface reconstruction engineering the associated electrocatalysts. For instance, light is widely used to drive the reaction in the energy conversion devices [12, 13]. Surface plasmon resonance (SPR) effect is originated from the collective oscillation of the valence electrons with certain frequency around the nanoparticle when the particles interact with incident light [14,15]. In this process, energetic electrons are excited and transferred to the nearby conductive or semiconductive materials [16], and meanwhile energetic holes are left on the surface of plasmonic nanostructures, which are potential to extract electrons from the surface of catalysts [17]. The commonly used plasmonic materials in electrocatalysis are noble metals [18], for example, Ni(OH)₂-Au catalyst was reported to show plasmon-promoted catalytic performance under irradiation of 532 nm laser [19], and the Au decorated MnO₂ nanosheets displayed enhanced activity under green light *via* forming the active Mnⁿ⁺ species [20]. Thus, it would be effective to apply SPR effect on metal borides to enlarge the extent of surface reconstruction to

* Corresponding authors.

E-mail addresses: dchen_80@hotmail.com (D. Chen), qinlaishun@cjlu.edu.cn (L. Qin), wen@fjirsm.ac.cn (Z. Wen).

accelerate active species generation.

It is very important to properly facilitate the surface reconstruction of catalysts, especially for those have high specific surface area (e.g., two-dimensional (2D) materials), which prefers to undergo a moderate surface reconstruction process without sacrificing all the bulk structure where the active sites are derived from [21]. However, the noble metal based plasmonic materials are high-cost, and it is difficult to regulate the intensity of SPR effect to avoid excessive reconstruction. We are therefore engaged in seeking plasmonic materials with tunable SPR effect. Molybdenum dioxide (MoO_2) with metallic character has been reported to have strong SPR effect under visible light as it possesses high density of d-orbit free electrons [22] which are induced by the rich oxygen vacancies [23]. As the oxidation state of Mo atom increases, the decrease in concentration of oxygen vacancies leads to diminished SPR effect [24, 25].

In this work, MoO_2 nanospheres exert the SPR effect on the 2D amorphous cobalt iron boride (CoFeB) nanosheets to achieve the function of accelerating and self-terminating surface reconstruction. We demonstrate that the strong SPR effect of MoO_2 nanospheres generates energetic electrons that are transferred to the Ni foam and further to the external circuit; the holes left accelerate the conversion of inactive Co^{2+} species to active cobalt oxyhydroxides on the surface of CoFeB under visible light, i.e., the SPR effect provides an additional acceleration for surface reconstruction under anodic voltage (Scheme 1). The density of state (DOS) of orbital around Fermi level (E_F) also suggests the Co on CoFeB-water interface will be more primarily to be oxidized into Co^{3+} . Such a reconstruction behaviour would be self-terminated to attain a stable reaction interface as the anodic voltage increases to thoroughly oxidize the MoO_2 to high valence state (MoO_3 , even MoO_4^{2-} to diffuse to electrolyte [26]). Additionally, we also unravel the real reactive surface for CoFeB during surface reconstruction is in the form of CoFeOOH with absorbed BO_2^- and prove the positive effect of BO_2^- on promoting the OER activity. The $\text{MoO}_2/\text{CoFeB}$ nanohybrids show a low overpotential (209 mV at $J=10 \text{ mA cm}^{-2}$) with the assistance of SPR effect. The application of Mo-based plasmon regulated surface reconstruction gives more possibilities for achieving highly active OER process.

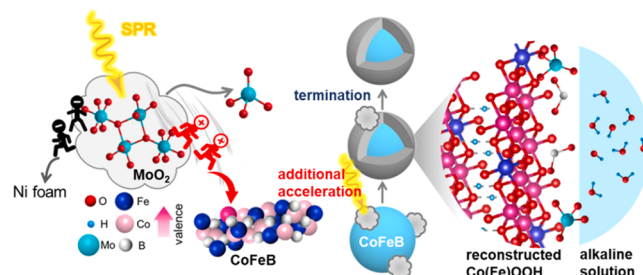
2. Experimental section

2.1. Synthesis of molybdenum dioxide (MoO_2) nanospheres

0.2 g of molybdenyl acetylacetone was dissolved in a mixed solution of deionized water (80 mL) and absolute ethanol (10 mL), and was then under stirring for 2 h at room temperature. Next, the mixture was transferred into a Teflon-lined stainless steel autoclave and held at 180 °C for 20 h. Finally, the products were washed by deionized water, collected by centrifugation and dried under vacuum to obtain black powders.

2.2. Synthesis of the binary cobalt iron boride (CoFeB) nanosheets

CoFeB nanosheets was prepared by chemical reduction method. Co



Scheme 1. Schematic illustration of the plasmonic MoO_2 regulated surface reconstruction and OER process for amorphous CoFeB Nanosheets.

($\text{NO}_3)_2\cdot 0.6 \text{ H}_2\text{O}$ (0.0067 M) and $\text{FeSO}_4\cdot 0.7 \text{ H}_2\text{O}$ (0.0033 M) were dissolved in a 100 mL of deionized water under ice bath to form a clear solution. Excess NaBH_4 (0.6 M, 5 mL) solution was slowly syringed into the mixture under ice bath in the protection of N_2 atmosphere. The precipitates was generated rapidly, washed by ethanol and deionized water sequentially, separated by centrifugation and dried under vacuum overnight.

2.3. Synthesis of $\text{MoO}_2/\text{CoFeB}$ hybrid heterostructure

The CoFeB nanosheets were dispersed in ethanol solution to form a homogenous ink-like mixture, and then the as-prepared MoO_2 nanospheres were added to it with the mass ratio of 5 wt %. After stirring for 1 h, the hybdrids were collected by centrifugation and dried under vacuum.

2.4. Characterizations

The crystal phases of the samples were recorded by X-ray diffractometer (XRD) (Ultima IV, Rigaku, Japan). The morphologies of the samples were obtained by the transmission electron microscope (TEM) (JEM-2010 F, JEOL, Japan) and scanning electron microscope (SEM) (Quanta 650, FEI, America). Chemical valence analysis was performed by X-ray photoelectron spectroscopy (XPS) (Escalab 250Xi, Thermo Scientific, America), and the XPS spectra were referenced to C 1 s emission at 284.8 eV. The UV-vis-NIR absorption spectra of the samples were recorded via a UV-visible-NIR spectrophotometer (UV-3600, Shimadzu, Japan). The evaluations of electrochemical activities were performed by an electrochemical workstation (CHI 660E, Chenzhua, China). EPR spectra were recorded on a electron paramagnetic resonance spectrometer (A300, Bruker, Germany) at room temperature with or without light irradiation (Xenon lamp+L42 cutoff filter).

2.5. Electrochemical measurements

To prepare the catalyst ink, 5 mg of catalyst powder was dispersed in ethanol (380 μL), and then 20 μL of Nafion solution (5 wt %, Dupont) was added to this suspension. After ultrasonic stirring for 30 min, 80 μL of the homogeneous ink was deposited onto a clean 1 cm \times 1 cm Ni foam substrate (catalyst loading: 1.0 mg cm^{-2}) to construct a work electrode.

Electrochemical performance was evaluated in a three-electrode configuration by electrochemical workstation. All the measurements were carried out in 1.0 M KOH aqueous solution. The reference electrode was a Ag/AgCl (3 M KCl) electrode, and the counter electrode was a graphite rod electrode. All the potentials in this work were normalized to a reversible hydrogen electrode (RHE) scale according to the Nernst equation: $E(\text{vs RHE}) = E(\text{vs Ag/AgCl}) + 0.059 \times \text{pH} + 0.198$. The OER polarization activity was measured by linear sweep voltammetry (LSV) with a scan rate of 5 mV s^{-1} at room temperature with and without visible light irradiation (Xenon lamp+L42 cutoff filter), and the power intensity of the incident light is 105.1 mW cm^{-2} that was measured by an optical power meter (CEL-NP2000-2, China Education Au-light Technology Co., Ltd). All the LSV curves are iR corrected by compensating the series resistance (R_s) values which were extracted from electrochemical impedance spectroscopy (EIS). Double-layer capacitance (C_{dl}) values were deduced from cyclic voltammetry (CV) measurements which were cycled between 1.15 and 1.25 V (vs RHE) at different scan rates. The electrochemical impedance measurement was evaluated at 1.50 V (vs RHE) from $1 \times 10^6 \text{ Hz}$ to 0.1 Hz in the same configuration as LSV measurements.

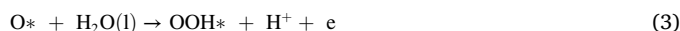
2.6. DFT details

All the DFT calculations are implemented via the Quantum Espresso [27]. Spin-polarized DFT calculations were performed with periodic

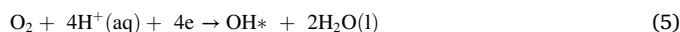
super-cells under the generalized gradient approximation (GGA) using the Perdew-Burke-Ernzerhof (PBE) functional for exchange-correlation and the ultrasoft pseudopotentials for nuclei and core electrons. The suggested kinetic energy and charge-density cutoff by pseudo producers are 64 Ry and 782 Ry, as inferred by the element has the largest cutoff value. But through a test, we find that values of 30 Ry and 300 Ry can also reach enough precision (<0.001 eV in relative energy), but with much lower computational cost. So 30 Ry and 300 Ry are used during computation. The Fermi-surface effects were treated by the smearing technique of Methfessel and Paxton, using a smearing parameter of 0.02 Ry. For all of the structures, the convergence criteria are set as 10^{-4} Ry/Bohr of Cartesian force components acting on each atom and 10^{-4} Ry of total energy. For all the structures, the 001 surface was cleaved as the study surface. During OER, catalyst will go through a surface oxidation. We use the reactions Gibbs energies (ΔG) of $\text{H}_2\text{O} \rightarrow * + 2\text{H}^+ + 2e^-$ and $* \rightarrow \text{H}^+ + e^-$ to discuss the possible oxidation/deoxidation and protonation/deprotonation that take place on the surface. When $\Delta G > 0$, it means surface will be reduced, or go through a protonation reaction; When $\Delta G < 0$, the surface will be oxidized, or go through a deprotonation reaction. This calculation is done iteratively until an equilibrium is reached. And we will use this obtained surface as the surface for OER study. Consequence, we found all the OH on CoFeOOH and CoFeOOH-BO₂ will be deprotonated to form O. We will hence use this structure as the surface to study the OER. Slab models with 6.33 Å × 6.33 Å R60° was use as the models for CoFeOOH, while that of 10.52 × 6.07 R90 as set as the model of CoFeOOH-BO₂. Two layers of structures are built, with the bottom layer remain fixed during the optimization. Vacuum layers with thickness of 13 Å was built for each surface. K point was set automatically by the program, which ensures the convergence in higher k points. And we double the k point when calculating the DOS. When optimizing BO₂⁻, one net charge is added into the BO₂⁻.

2.6.1. OER mechanism and the proposition of the free energy diagram

When discussing the OER mechanism, the OER is assumed to follow a classical 4 proton coupled electron transfer (PCET) process [28] that is written as:



The asterisk stands for the site on the surface of a certain catalyst. The free energies of O_{2(g)} are calculated by the equilibrium of:



on 1.23 V to avoid the error of DFT energy caused by the high spin of O₂ [27,28]. The chemical potential of H⁺(aq) is calculated by the 1/2 H₂(g) on the basis of computational hydrogen electrode (CHE) method [29].

The chemical potentials of adsorbates X* is calculated by the following expression:

$$\mu_{X*} = E_{X*} - E_* + ZPE_{X*} - TS_{X*} \quad (6)$$

The E_{X*} and E_* are the DFT based total energies of active sites with and without the adsorbates X*. The ZPE and TS are the contributions from zero points and entropies of adsorbates, whose values are listed on Table S1. The formation free energy of OH*, O* and OOH*, denoted as $G_{\text{OH}*}$, $G_{\text{O}*}$ and $G_{\text{OOH}*}$, are defined as:

$$G_{\text{OH}*} = \mu_{\text{OH}*} + 1/2\mu_{\text{H}_2*} - Ue - \mu_{\text{H}_2\text{O}} \quad (7)$$

$$G_{\text{O}*} = \mu_{\text{O}*} + \mu_{\text{H}_2*} - 2Ue - \mu_{\text{H}_2\text{O}} \quad (8)$$

$$G_{\text{OOH}*} = \mu_{\text{OOH}*} + 3/2\mu_{\text{H}_2*} - 3Ue - 2\mu_{\text{H}_2\text{O}} \quad (9)$$

U is set as 1.5 V when proposing the FED. The associated $G_{\text{OH}*}$, $G_{\text{O}*}$ and $G_{\text{OOH}*}$ values for picked sites are gathered in Table S1.

2.6.2. Calculations of Fermi level

Commonly, when talking about the Fermi level, we use vacuum infinity as the reference state, i.e., the zero point. However, things are a little different in plane-wave basis DFT calculation, in which we used periodic boundary condition (pbc). Under pbc, the electron energy level at infinity is also zero, but this “infinity” is not the “vacuum infinity”, it is the “pbc infinity”. The same part for “vacuum infinity” and “pbc infinity” is they are both the reference state for calculated Fermi level (reference state means their levels are both zero). However, the most important difference between the “pbc infinity” and the “vacuum infinity” lies on the path: the path moving an electron from the study materials to the “pbc infinity” is different from that to the “vacuum infinity”. Since energy value is calculated by the integration of the reversible work along the path, so if one uses pbc condition, the energy level of “pbc infinity” should be different from that of the “vacuum infinity”. And only the latter is physically meaningful. Therefore, in pbc based DFT, if one needs to get the meaningful Fermi level, one cannot use that value output by DFT software, instead, one should try to calculate the level of vacuum infinity, i.e., vacuum energy level. To do this, one needs to know the component of the energy difference between vacuum level (E_{vac}) and Fermi level (E_f). It is composed by three terms:

$$E_f - E_{\text{vac}} = u_e + e\Delta\chi + e\varphi \quad (10)$$

where u_e , $\Delta\chi$ and φ are the chemical potential, surface potential difference and the so-called “outer potential”. The sum of the first two terms is the energy gained if we move an electron at the surface to the bulk. The third term are caused by the net charge or net dipole moment carried by the material. In practical situation, the third term should be zero because of the screen effect by the ions and water molecules. But in DFT, this term will remain in a default situation. So if we can diminish the third term, they we can simply calculate the spatial dependent electrostatic potential in DFT box, and set any point outside the material as the “vacuum energy”, and obtain the Fermi level. So how to diminish it? in the early time, they can be cancelled by using a “double reference model” that we build a symmetrical model to cancel the φ . However, this method is quite inconvenient. Recently, the effective screen medium (ESM) method proposed by Otani [30] provides a simpler solution. It directly wipes the contribution of electrostatic potential from other pbc, thus wipe the possible φ . This ESM method is also used in this paper. So we can achieve the E_f for any given structures.

2.6.3. Fermi level and DOS of amorphous structures

CoFeB is amorphous, despite we have already achieved its structures [31], such structure is large and we cannot directly model it in calculating DOS and Fermi level. Therefore, we should use “cut model” to get an ensemble of the structures. And calculate the E_f and DOS from the average of these structures. 50 surface structures were used to calculated E_f , while 50 randomly picked atoms are used to calculated DOS.

2.7. Photovoltaic-water splitting test

A commercial three junction GaInP/GaInAs/Ge solar cell (0.85 cm⁻²) with an open-circuit voltage (V_{oc}) of 2.46 V and a short-circuit current (I_{sc}) of 9.6 mA was used as the power input under the irradiation of an AM 1.5 G solar simulator (XES-50S1-RY, San-Ei Electric Co., Japan), which was selected as the photovoltaic device.

The solar to hydrogen conversion efficiency (η) was calculated as below:

$$\eta (\%) = \frac{P_{out}}{P_{in}} \times 100\% = \frac{J_{op} [\text{mA cm}^{-2}] \times FE_{hydrogen} \times E_{hydrogen}^0}{P_{solar} [\text{mW cm}^{-2}]} \times 100\%$$

J_{op} means the operating current density in the working system, where the geometric area of solar cell is 0.85 cm^2 . $E_{hydrogen}^0$ is thermodynamic potential for hydrogen equals to 1.23 V and P_{solar} is the power of input solar (100 mW cm^{-2}).

3. Results and discussion

3.1. Synthesis and structural characterizations

Fig. 1a exhibits the synthetic route to MoO_2 nanospheres decorated CoFeB nanosheets. The MoO_2 nanospheres were prepared by hydrothermal method. Subsequently, cobalt iron boride (CoFeB) nanosheets were synthesized by chemical reduction method with the NaBH_4 as both reductant and boron resource. The $\text{MoO}_2/\text{CoFeB}$ nanohybrids were finally obtained through physically assembly induced by electrostatic interaction in the solution. As revealed by scanning electron microscopy

(SEM) (Fig. S1a) and transmission electron microscopy (TEM) (Fig. S1b) images, the MoO_2 are nanospheres with diameters of 50–80 nm, and the high-resolution TEM (HRTEM) image (Fig. S1c) shows clear lattice fringe of 0.342 nm, consistent with the (011) plane of monoclinic MoO_2 [22]. The CoFeB shows morphology of nanosheet (Fig. S2a) and HRTEM image (Fig. S2b) exhibits amorphous feature without obvious lattice fringe. Fig. 1b and c are the TEM and HRTEM images for the $\text{MoO}_2/\text{CoFeB}$ nanohybrids, respectively. It is clear that MoO_2 nanospheres are loaded on the CoFeB nanosheets and the two parts can also be evidently distinguished in the HRTEM image according to their difference on crystallinity. Elemental mapping (Fig. 1d) shows uniform dispersion of Co, Fe, and B elements in the nanosheet structure and Mo element in the isolated spherical structure. The element of O is distributed throughout the hybrids due to the surface oxidation and the O signal in the spherical structure (corresponds to MoO_2) is much stronger than that in the nanosheet structure. The XPS survey scan spectra (Fig. S3) of the samples also manifest the existence of Co, Fe, B, Mo, and O elements. XRD patterns confirms the amorphous phase of CoFeB (Fig. 1e) [32] and the crystalline phase of monoclinic MoO_2 (JCPDS No. 78-1069) (Fig. S4)

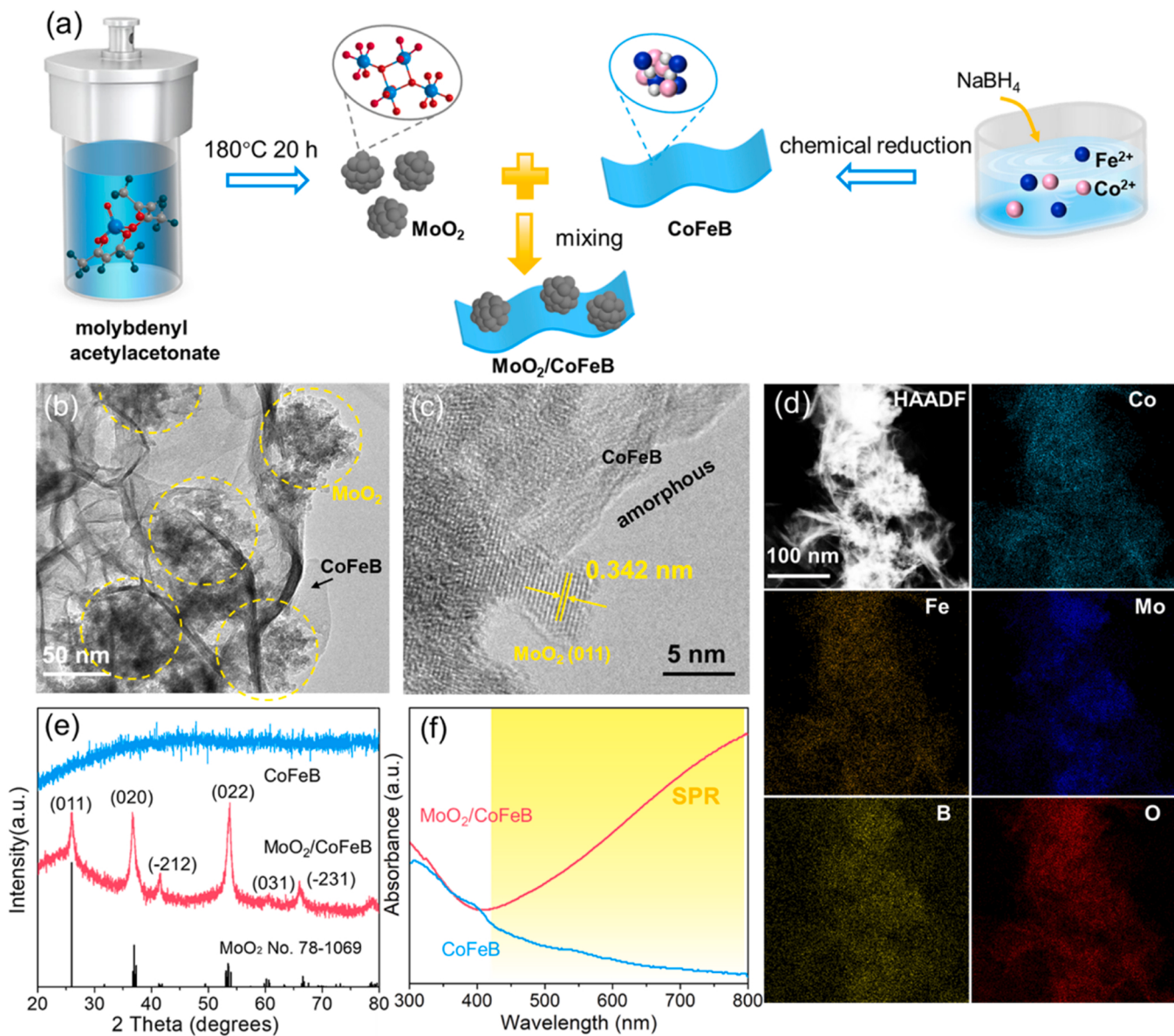


Fig. 1. (a) Illustration of the synthetic route of $\text{MoO}_2/\text{CoFeB}$ catalyst. (b) TEM and (c) HRTEM images of $\text{MoO}_2/\text{CoFeB}$ catalyst. (d) Element mapping of the $\text{MoO}_2/\text{CoFeB}$. (e) XRD patterns and (f) UV-vis absorption spectra of CoFeB and $\text{MoO}_2/\text{CoFeB}$ catalysts.

[22], consistent with the HRTEM results, while the MoO₂/CoFeB nanohybrids consist of both phases. Additionally, the light absorption properties of CoFeB nanosheets and the MoO₂/CoFeB nanohybrids were further examined by UV-vis absorption spectroscopy in Fig. 1f. The CoFeB shows very weak absorption in the region of visible light. In contrast, the MoO₂/CoFeB nanohybrids display distinct localized surface plasmon resonance (SPR) absorption band that is derived from the plasmonic MoO₂ (see the light absorption spectrum in Fig. S5) [23].

3.2. Electrocatalytic performance for OER

We next tested the OER catalytic performance of CoFeB nanosheets and MoO₂/CoFeB nanohybrids with and without visible light excitation in a three-electrode electrochemical cell at room temperature. The Co to Fe ratio in the binary metal borides has been optimized before (Fig. S6). With the MoO₂ nanospheres loading, MoO₂/CoFeB nanohybrids do not exhibit obvious improvement in OER activity (Fig. 2a), and both require overpotential of 252 mV to reach the current density of 10 mA cm⁻² (Fig. 2b). Upon irradiation with visible light for 5 min, the OER activity of MoO₂/CoFeB nanohybrids show an evident improvement compared to the dark condition, with a precipitously dropped overpotential of 209 mV, although the CoFeB nanosheets display much smaller enhancement (the overpotential is reduced from 252 to 240 mV). The amount of MoO₂ loading has also been optimized (Fig. S7), and the 5 wt % loading of MoO₂ shows the best SPR enhanced performance. The performance of MoO₂/CoFeB under light excitation surpasses most of the plasmon enhanced catalysts, Fig. S8). Nyquist plots (Fig. 2c)

measured from electrochemical impedance spectroscopy (EIS) reveal that the semicircular diameter of the MoO₂/CoFeB nanohybrids is obviously decreased with the light irradiation while the extent of decrease is smaller for the CoFeB nanosheets, indicating the conductivity is facilitated by the light induced SPR effect of MoO₂. The parameters for resistance elements of the equivalent circuit are shown in Table S2, indicating the MoO₂/CoFeB under light irradiation exhibits the lowest charge-transfer resistance (R_{ct}). As for the Tafel plots (Fig. 2d), the Tafel slopes of CoFeB and MoO₂/CoFeB samples are decreased from 54.8 to 48.1 and 44.5 mV dec⁻¹ respectively after light irradiation, further suggesting that the kinetics promotion is owing to the SPR excitation of the MoO₂ nanospheres. Therefore, under the dark condition, the MoO₂ loading makes no difference in catalytic performance while the SPR effect under light contributes a lot. Hence the MoO₂/CoFeB nanohybrids with and without light irradiation are further investigated. Moreover, the MoO₂/CoFeB nanohybrids possess good stability under visible light during the chronopotentiometry measurement (Fig. S9). TEM images show the structure of nanospheres loading on nanosheets can still be observed (Fig. S10a-b), confirming that the morphology of the catalyst was largely retained during the stability test. The HRTEM image (Fig. S10c) shows the interplanar distance of 0.216 nm, corresponding to the (102) plane of CoOOH that is produced after the surface reconstruction, and the Raman spectrum also shows the feature peak of CoOOH (Fig. S11). In the high-resolution Co 2p spectrum (Fig. S12a), the peak at binding energy of 780.1 eV corresponds to the Co³⁺ for CoOOH. The peak at binding energy of 529.6 eV that represents the O in OOH species also enhanced after the stability test (Fig. S12b).

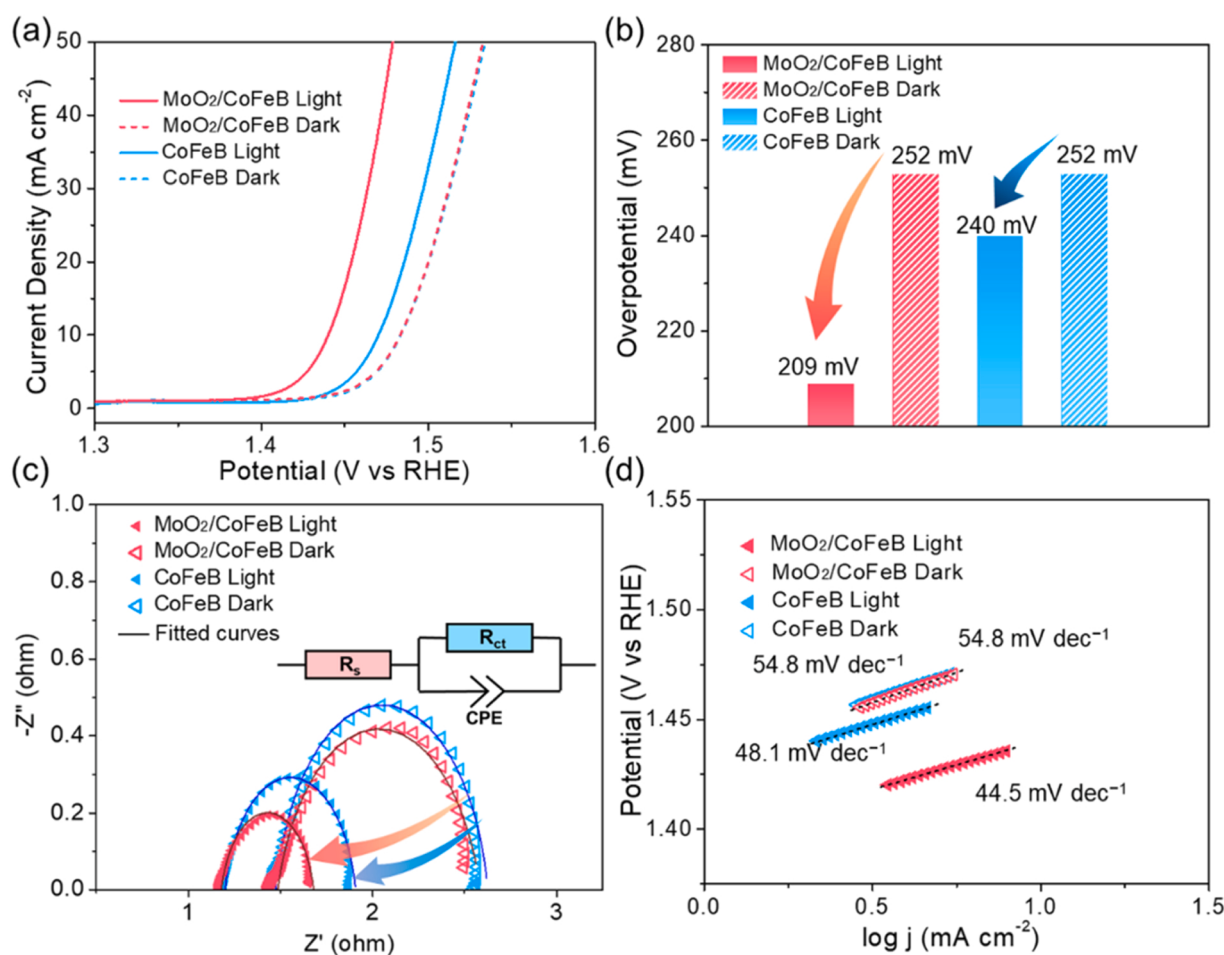


Fig. 2. (a) OER polarization curves (with iR -correction, scan rate: 5 mV s⁻¹), (b) overpotentials at current density of 10 mA cm⁻², (c) EIS Nyquist plots (the inset is the equivalent circuit: R_s series resistance, R_{ct} charge-transfer resistance, and CPE constant-phase element related to the double-layer capacitance) and (d) Tafel plots for OER on CoFeB and MoO₂/CoFeB catalysts in 1.0 M KOH electrolyte with (denoted as Light) and without (denoted as Dark) visible light irradiation.

The Fe 2p spectrum (Fig. S12c) shows the peak at 711.5 eV for the Fe^{3+} , which is consistent with the pre-OER sample. The signal of Mo 3d XPS spectrum (Fig. S12d) is weak because the surface-reconstructed oxy-hydroxide nanosheets wrap around the Mo species. Under anodic voltage, the MoO_2 surface undergoes the excitation of hot electrons and surface oxidation, which induce lower-valent Mo (*i.e.*, Mo^0) and the higher-valent Mo (MoO_4^{2-} or MoO_3), respectively.

3.3. Exploration of the SPR effect regulated OER process

To get insights into the influence of anodic scanning and SPR on the surface reconstruction for $\text{MoO}_2/\text{CoFeB}$ nanohybrids, X-ray photoelectron spectroscopy (XPS) measurements were conducted to figure out the change of surface electronic structure under anodic voltage and light irradiation. The as-prepared $\text{MoO}_2/\text{CoFeB}$ firstly shows binding energy of Co 2p_{3/2} peak at 781.2 eV (Fig. 3a), mainly attributed to the Co^{2+} in CoO species at surface [33,34]. The peaks (located at 711.9 and

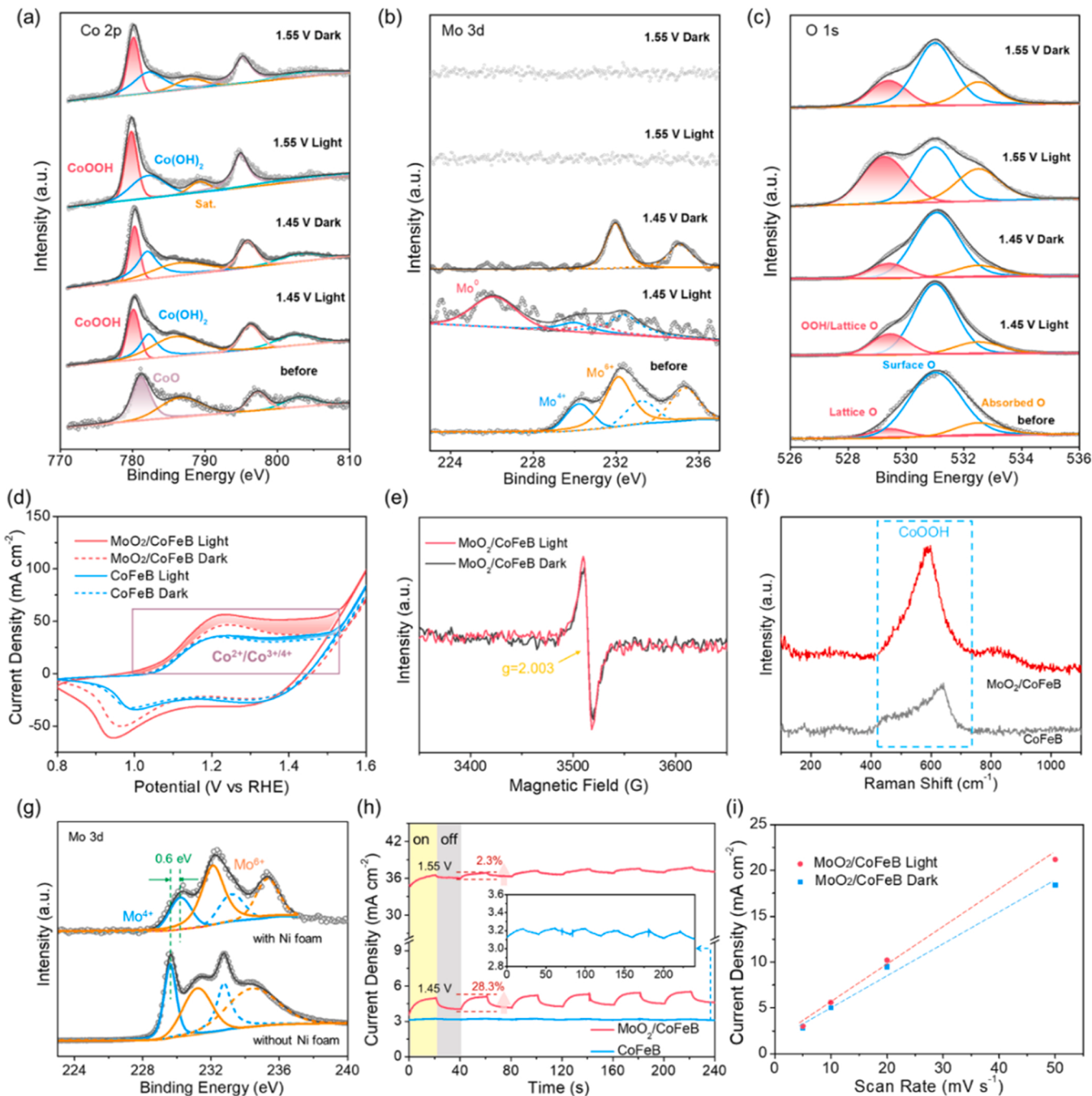


Fig. 3. (a) Co 2p, (b) Mo 3d, (c) O 1s XPS spectra of $\text{MoO}_2/\text{CoFeB}$ catalyst before OER and operated under different anodic voltages with (denoted as Light) and without (denoted as Dark) visible light irradiation. (d) CV curves of CoFeB and $\text{MoO}_2/\text{CoFeB}$ catalysts with (denoted as Light) and without (denoted as Dark) visible light irradiation. Scan rate: 100 mV s^{-1} . (e) Room-temperature ESR spectra for $\text{MoO}_2/\text{CoFeB}$ catalyst with and without light excitation (Xenon lamp+L42 cutoff filter). (f) Raman spectra of the post-OER $\text{MoO}_2/\text{CoFeB}$ nanohybrids and CoFeB (1.45 V vs RHE, with light irradiation). (g) Mo 3d XPS spectra for the $\text{MoO}_2/\text{CoFeB}$ hybrids with and without Ni foam substrate. (h) Chronoamperometric i - t curves of the catalysts under chopped irradiation at different anodic voltages. The inset is the enlarged graph of i - t curve for CoFeB . (i) The differences in current density (Δi) at 1.20 V vs RHE plotted against scan rate fits to a linear regression for $\text{MoO}_2/\text{CoFeB}$ with and without light irradiation.

724.9 eV) in Fe 2p spectra (Fig. S13) are assigned to high valence Fe^{3+} [35]. Compared with the single CoFeB, the MoO_2 loading under dark condition did not induce obvious changes to the electronic structure for Co and Fe sites (Fig. S14), so the SPR effect under light plays a major role in the improvement of OER activity. The Mo 3d spectrum is deconvoluted into two pairs of peaks (Fig. 3b), corresponding to Mo^{4+} (230.1 eV, 232.7 eV) and Mo^{6+} (231.9 eV, 235.2 eV) [36,37]. The O 1 s XPS spectrum (Fig. 3c) exhibits three peaks at 529.4, 531.0 and 532.5 eV, which are mainly assigned to lattice O in MoO_2 , surface O and absorbed O of the CoFeB surface, respectively [38]. In addition, the B 1 s spectrum (Fig. S15) shows peaks at binding energies of 187.7 (M-B bond) and 191.7 eV (B-O bond) [10], and the strong signal of B-O also manifests the metal boride undergoes surface oxidation.

We then applied an anodic voltage of 1.45 V (vs RHE) which is smaller than the end potential of Co^{2+} to $\text{Co}^{3+/4+}$ oxidation peak (in the range of 1.0–1.53 V vs RHE, Fig. 3d) in cyclic voltammogram (CV) [39], attempting to promote the valence transition for surface reconstruction. As shown in Fig. 3a, both the binding energies of Co 2p_{3/2} for MoO_2 /CoFeB nanohybrids with and without light irradiation are shifted negatively after applied anodic voltage of 1.45 V (vs RHE), which manifests the surface valence change. The peaks of Co 2p_{3/2} level are deconvoluted into two distinct species at 780.1 and 782.2 eV, correspond to the formation of cobalt oxyhydroxide (CoOOH) and cobalt hydroxide (Co(OH)_2) [26,33], respectively. The Raman spectra (Fig. S16) for the post-OER sample of MoO_2 /CoFeB shows the peak at 587 cm⁻¹ (corresponded to the CoOOH), which also confirms the formation of oxyhydroxides. The morphological features of catalysts under 1.45 V (vs RHE) are shown in Fig. S17 and S18. As shown, the continuous nanosheets features are kept except that some weak crystalline patterns emerge in the HRTEM image, indicating the lamellar oxyhydroxides are generated on the surface of CoFeB. For the nanohybrids of MoO_2 /CoFeB, the edges of MoO_2 nanospheres are faded (marked by the dashed yellow circle) due to the surface oxidation under anodic voltage. These results indicate the anodic voltage can drive the surface reconstruction and low-valent Co species is mainly converted to active CoOOH . The ratios of CoOOH to other Co species from the Co 2p spectra were calculated and shown in Table S3, which reveals that under light more CoOOH is produced than the dark condition. We further investigated the O 1 s spectra under the anodic voltage of 1.45 V (vs RHE), and the peaks (at around 529.4 eV) related to oxyhydroxide are obviously increased, among which the light condition is more remarkable (the ratios of O species are listed in Table S4). This result is consistent with the inference of Co 2p spectra, demonstrating that the light excitation induces enhanced surface reconstruction for the CoFeB. Clearly, upon the anodic voltage of 1.45 V, surficial Mo^{4+} atoms are oxidized to become Mo^{6+} (in the forms of MoO_3 and MoO_4^{2-}) without light irradiation, while a few lower valence state of Mo atoms (226.2 eV) appear under visible light. Electron paramagnetic resonance (EPR) spectra (Fig. 3e) further confirm this consequence because the signal ($g=2.003$) for oxygen vacancy in MoO_2 is enhanced under light [40], which also represents the decrease of valence state for Mo [41]. Such changes in chemical state of Mo atoms signify that the electrons are excited in the MoO_2 via visible light induced SPR effect. Besides, the Raman spectra (Fig. 3f) for the post-OER MoO_2 /CoFeB under light shows enhanced signals of CoOOH compared with the CoFeB sample, which also manifests the hot electrons are excited through SPR effect of the remained Mo oxides to enhance the Raman signals. We also observe that the chemical valence of Mo (Fig. 3g) in MoO_2 /CoFeB powders is lower than that loaded on Ni foam, which means the Ni foam is potential to get electrons from element Mo. Therefore, when driven by the electric field, we reasonably infer that the energetic electrons are generated under light and could be transferred to Ni foam, and subsequently to the external circuit, and hence the holes left may accelerate the oxidation of low valent Co species.

Moreover, CV curve reflects the oxidation process of surficial low-valent metal species [42,43]. In view of that the Fe atoms in the

CoFeB nanosheets are already in high valence state, the anodic oxidation peak is mainly ascribed to the transform of Co^{2+} to $\text{Co}^{3+/4+}$ (Fig. 3d) [39,44]. The area between dash line and solid line arises from the impact of visible light. As for the MoO_2 /CoFeB nanohybrids, the oxidation peak is positively shifted and the peak area is slightly increased compared with the CoFeB, indicating some of the MoO_2 nanospheres are oxidized. With the light irradiation, the area between the dash line and solid line is evidently larger than that of the dark condition, which verifies the contribution of SPR effect for accelerating the oxidation of inactive Co^{2+} species to $\text{Co}^{3+/4+}$. To further verify the instant photoresponse of MoO_2 /CoFeB nanohybrids over OER electrocatalysis, the *i-t* curves under 1.45 V vs RHE with irradiation switched on and off are shown in Fig. 3h. As expected, negligible photoresponse current of CoFeB nanosheets under visible light irradiation is observed, while MoO_2 /CoFeB nanohybrids show a rapidly increased current under light irradiation and the oxygen evolution is restricted when switching off the light.

When the applied voltage further increases to 1.55 V vs RHE (smaller than which the Co oxidation process has already been completed), the signals related to CoOOH in Co 2p spectra (Fig. 3a) and OOH in O 1 s spectra (Fig. 3c) are obviously enhanced compared with they do under lower anodic voltage (quantitative data for different Co and O species deduced from XPS data are shown in Table S3 and S4), which means more surficial metal oxyhydroxides (CoOOH) are produced. The element Fe with and without light excitation is still in the form of high valent Fe^{3+} (Fig. S13). However, the Mo 3d signals (Fig. 3b) are difficult to detect, which results from that large amount of MoO_2 nanospheres are oxidized to MoO_4^{2-} and further diffusing to electrolyte, consistent with the previous report about Mo based materials [26]. In this instance, the SPR induced effect is dramatically weakened. The response of the catalyst under visible light irradiation tends to be negligible (Fig. 3h): the current increment for hybrids under 1.55 V vs RHE (2.3 %) during 20 s is much lower than that for 1.45 V vs RHE (28.3 %). Hence the SPR induced acceleration towards surface reconstruction for CoFeB nanosheets could be self-terminated to avoid the dissociation of bulk catalyst caused by excessive reconstruction. As supplementary, the electrochemical active area (ECSA) was calculated from the cyclic voltammetry (Fig. S19) at different scan rates within the non-Faradaic potential range [45,46]. It is clear that the ECSA of MoO_2 /CoFeB nanohybrids with light irradiation is relative larger than that without light irradiation (Fig. 3i), in other words, the surface reconstruction does not compromise all the bulk of the high specific surface catalyst to lose the reactive interface.

3.4. Theoretical computation

We introduce first-principle based analysis to understand the charge transfer and active species conversion of the MoO_2 /CoFeB. We first found for all the three phases, namely, MoO_2 , CoFeB, and Ni, their electron density of state (DOS) pictures all show an overlap of the valence band and the conduction band (Fig. 4a). This indicates these three phases in bulk are all conductors to electrons and holes. On the other hand, considering the concerned interphases here are the MoO_2 /Ni and MoO_2 /CoFeB, it is then necessary to discuss whether these two interphases are still conductors. For the former, the MoO_2 /Ni interphase, we straightforwardly build an interfacial model that contains MoO_2 and Ni phases and calculate their DOS. We found the total DOS shows overlap of the valence band and the conduction band, and the pDOS of interfacial Mo, O and Ni all shows unoccupied orbitals around the Fermi level (Fig. 4b). This suggests MoO_2 /Ni interphase is also the conductors. On the other hand, as for the MoO_2 -CoFeB interface, since CoFeB is amorphous, it is inappropriate to directly model a MoO_2 -CoFeB interface in DFT. So as an alternative, we calculate the Fermi energies of amorphous CoFeB and MoO_2 (see details in Sections 2.6.2–2.6.3). It turns out that amorphous CoFeB is higher by about 1 eV, as indicated in Fig. 4c. Thus, when amorphous CoFeB contacts with MoO_2 , electron will spontaneously pass from amorphous CoFeB to MoO_2 to generate the bipolar layer to balance the electrochemical potential of electrons in

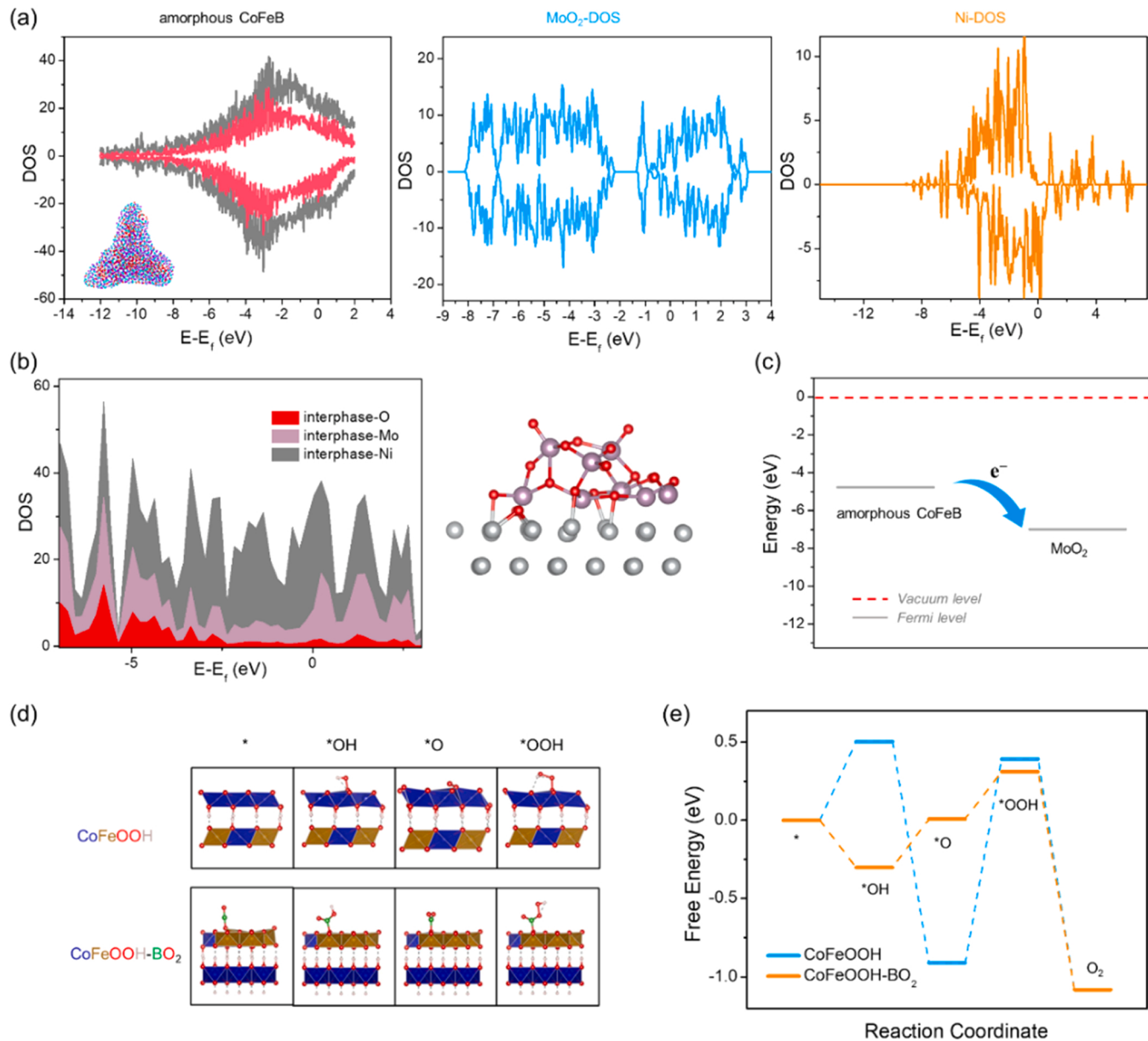


Fig. 4. (a) The DOS of amorphous CoFeB, MoO_2 and Ni. The amorphous CoFeB generated in our previous simulation is used (inset is element distribution for the simulated CoFeB, Ref.[30], the red, purple, and blue balls represent Fe, Co, and B elements). The method to calculate the amorphous CoFeB is given in Section 2.6.3. The total DOS of CoFeB is shown by gray line. The partial DOS of Co in CoFeB is shown by red line. (b) The partial DOS of O (red), Mo (purple) and Ni (gray) atoms in MoO_2/Ni interphase. The optimized structure of interphase is shown aside. (c) The Fermi level of amorphous CoFeB and MoO_2 . The calculation details of it, especially amorphous CoFeB are shown in Sections 2.6.2–2.6.3. (d) The side view of the reaction intermediates and (e) free energy diagrams of OER on CoFeOOH and CoFeOOH-BO₂.

both phases. In this case, if the carrier concentration in amorphous CoFeB is small, electron depletion will take place at the amorphous CoFeB side, generating a Schottky barrier to prevent electron coming from MoO_2 . However, since in this case it is the photogenerated hole transporting from MoO_2 to amorphous CoFeB, even if there exists a Schottky barrier, it won't prevent the transport of hole through the interface. That is, the higher E_f of amorphous CoFeB than MoO_2 can indicate no hinder for hole transportation on interface. Therefore, it is concluded the component of interphase, MoO_2/Ni and $\text{MoO}_2/\text{CoFeB}$, will both aid, or at least won't harm the transfer of photogenerated carriers. Additionally, as indicated by the pDOS of Co and the total DOS of CoFeB, most of the DOS around E_f of amorphous CoFeB are contributed by Co (Fig. 4b, 70 %). This indicates (1) when hole moved from MoO_2 to CoFeB, it will most likely locate on orbital contributed by Co,

(2) since the density of state of orbital around E_f can suggest the reactivity, the Co on CoFeB-water interface will be more primarily to be oxidized into Co^{3+} . This is consistent with the experimental results above.

During the surface reconstruction process, the M-B signal in B 1 s XPS spectra (Fig. S15) decreases with increasing the applied potential and only the signal of B-O remains at 1.45 V vs RHE, which implies the oxidation of B to borate. As the applied bias further increases, the signal of B related species is negligible. This phenomenon suggests the thoroughly oxidized surface B species (BO_2^- in alkaline condition) moves to the electrode-electrolyte interface and further diffuses to the electrolyte. To unveil the effect of surface absorbed BO_2^- , we also use DFT to understand the role of B in OER. The eventual structure for CoFeB is metal oxyhydroxide (CoFeOOH) with absorbed BO_2^- (denoted as CoFeOOH-

BO_2). The Norskov's approach [47] is introduced and the free energy diagrams (FED) of OER on corresponding surfaces, namely, the CoFeOOH, and CoFeOOH- BO_2 are calculated and plotted in Fig. 4d. The details are shown in Section 2.6.2. From it we see the impact of BO_2^- is critical. As shown in the orange FED in Fig. 4e, the activity of CoFeOOH- BO_2 has been greatly improved because the highest reaction free energy barriers on CoFeOOH- BO_2 is much smaller than that for CoFeOOH. Finally, the intrinsic reason for the activity enhancement by BO_2^- is because BO_2^- can provide additional site, i.e., the BO_2 site for OER. This site has a larger affinity to the OER intermediates, hence lower the "virtual energetic span" (denoted as δE_v) [48] of OER. Hence for the CoFeB boride catalyst, the moderately enhanced transformation of inactive Co^{2+} to active $\text{Co}^{3+/4+}$ coupled with surface absorbed BO_2^- species contributed to the greatly decreased overpotential for OER.

To verify the feasibility of the plasmon assisted OER as an effective anodic reaction of overall water splitting, we assembled a photovoltaic driven hydrogen production electrolyser with a three junction GaInP/GaInAs/Ge solar cell (the illuminated surface area is 0.85 cm^2) as the power input (Fig. S20a). The full-cell used $\text{MoO}_2/\text{CoFeB}$ as anodic electrocatalyst for OER and commercial Pt as cathodic electrocatalyst for hydrogen evolution, the 1 M KOH aqueous solution as the electrolyte, and the anodic anode was also excited by the light. From the current-voltage curve of the solar cell and the polarization curve of the constructed full-cell (Fig. S20b), the system outputs the current of 9.6 mA for hydrogen production. Over the period of 4 h, the current remains well at ~ 9.5 mA with average Faradaic efficiency for hydrogen of 95 % (Fig. S20c). On average, the solar to hydrogen (STH) conversion efficiency during the measurement is achieved to be 13.2 %.

4. Conclusion

In summary, we reported a SPR engineering method to regulate surface reconstruction of CoFeB nanosheets by decorating plasmonic MoO_2 nanoparticles, in which energetic electrons and holes were generated thanks to the SPR effect of MoO_2 , accelerating the conversion of inactive low-valent Co species to active cobalt oxyhydroxide for electrocatalysis of OER. The oxidation of MoO_2 and MoO_4^{2-} leaching weaken the SPR effect and quench the further SPR induced acceleration with maintaining a relative stable reaction interface. Furthermore, the absorbed BO_2^- on the reconstructed oxyhydroxide surface provide additional site to further lower the OER overpotential. This study may provide a promising strategy to regulate the dynamic reconstruction of electrocatalysts for advancing its catalytic activity toward a diversity of electrochemical applications.

CRediT authorship contribution statement

Huayu Chen: Conceptualization, Methodology, Data collection and curation, Data analysis and interpretation, Writing – original draft. **Junxiang Chen:** Theoretical model, DFT calculating, Writing – review & editing. **He He:** Characterization. **Xin Chen:** TEM characterization and analysis. **Chunguang Jia:** DFT calculating. **Da Chen:** Conceptualization, data analysis, discussion, writing. **Junhui Liang:** Electrochemical testing. **Dandan Yu:** Synthesis. **Xin Yao:** Characterization. **Laishun Qin:** Conceptualization for materials design and synthesis. **Yuexiang Huang:** data collection and analysis. **Zhenhai Wen:** Conceptualization, Writing, Revision.

Declaration of Competing Interest

The authors declare that they have no known competing financial interests or personal relationships that could have appeared to influence the work reported in this paper.

Data Availability

Data will be made available on request.

Acknowledgements

This work is financially supported by the National Natural Science Foundation of China (Nos. 51972294, 51872271, 21875253), the Natural Science Foundation of Zhejiang Province (Nos. LQ20F040007, LQ19F040004), the Open Fund Project of Key Laboratory of Jiangxi Province for Persistent Pollutants Control and Resources Recycle (Nanchang Hangkong University) (ES202180069), Scientific Research and Equipment Development Project of CAS (YJKYYQ20190007), and the Fundamental Research Funds for the Provincial Universities of Zhejiang (2022YW62, 2021YW35).

Authorship contribution statement

Huayu Chen conceived the idea, carried out the experiments and wrote the paper. Junxiang Chen and Chunguang Jia conducted the DFT calculations. Xin Chen and He He analyzed the data. Da Chen and Zhenhai Wen revised the paper. Junhui Liang, Dandan Yu, Xin Yao, Laishun Qin, and Yuexiang Huang helped the materials characterizations.

Appendix A. Supporting information

Supplementary data associated with this article can be found in the online version at doi:10.1016/j.apcatb.2022.122187.

References

- [1] F.S.M. Ali, R.L. Arevalo, M. Vandichel, F. Speck, E.-L. Rautama, H. Jiang, O. Sorsa, K. Mustonen, S. Cherevko, T. Kallio, Hydrogen evolution in alkaline medium on intratube and surface decorated PtRu catalyst, Appl. Catal. B 315 (2022), 121541.
- [2] Z.P. Yu, Y.F. Li, A. Torres-Pinto, A.P. LaGrow, V.M. Diaconescu, L. Simonelli, M. J. Sampaio, O. Bondarchuk, I. Amorim, A. Araújo, A.M.T. Silva, C.G. Silva, J. L. Faria, L.F. Liu, Single-atom Ir and Ru anchored on graphitic carbon nitride for efficient and stable electrocatalytic/photocatalytic hydrogen evolution, Appl. Catal. B 310 (2022), 121318.
- [3] Y. Yang, S. Wei, Y. Li, D. Guo, H. Liu, L. Liu, Effect of cobalt doping-regulated crystallinity in nickel-iron layered double hydroxide catalyzing oxygen evolution, Appl. Catal. B 314 (2022), 121491.
- [4] X. Han, N. Li, Y.B. Kang, Q. Dou, P. Xiong, Q. Liu, J.Y. Lee, L. Dai, H.S. Park, Unveiling trifunctional active sites of a heteronanosheet electrocatalyst for integrated cascade battery/electrolyzer systems, ACS Energy Lett. 6 (2021) 2460–2468.
- [5] N.C.S. Selvam, L. Du, B.Y. Xia, P.J. Yoo, B. You, Reconstructed water oxidation electrocatalysts: the impact of surface dynamics on intrinsic activities, Adv. Funct. Mater. 31 (2021), 2008190.
- [6] H. Huang, C. Yu, H. Huang, C. Zhao, B. Qiu, X. Yao, S. Li, X. Han, W. Guo, L. Dai, J. Qiu, Activation of transition metal oxides by in-situ electro-regulated structure-reconstruction for ultra-efficient oxygen evolution, Nano Energy 58 (2019) 778–785.
- [7] S. Wan, X. Wang, G. Zhang, Y. Wang, J. Chen, Q. Li, Y. Zhang, L. Chen, X. Wang, G. Meng, K. Jiang, ACS Sustain. Chem. Eng. 10 (2022) 11232–11241.
- [8] Y. Li, Y. Wu, H. Hao, M. Yuan, Z. Lv, L. Xu, B. Wei, In situ unraveling surface reconstruction of $\text{Ni}_5\text{P}_4/\text{FeP}$ nanosheet array for superior alkaline oxygen evolution reaction, Appl. Catal. B 305 (2022), 121033.
- [9] J. Wang, S.-J. Kim, J. Liu, Y. Gao, S. Choi, J. Han, H. Shin, S. Jo, J. Kim, F. Ciucci, H. Kim, Q. Li, W. Yang, X. Long, S. Yang, S.-P. Cho, K.H. Chae, M.G. Kim, H. Kim, J. Lim, Redirecting dynamic surface restructuring of a layered transition metal oxide catalyst for superior water oxidation, Nat. Catal. 4 (2021) 212–222.
- [10] J. Masa, P. Weide, D. Peeters, I. Sinev, W. Xia, Z. Sun, C. Somsen, M. Muhler, W. Schuhmann, Amorphous cobalt boride (Co_2B) as a highly efficient nonprecious catalyst for electrochemical water splitting: oxygen and hydrogen evolution, Adv. Energy Mater. 6 (2016), 1502313.
- [11] Y. Zhang, C. Liang, J. Wu, H. Liu, B. Zhang, Z. Jiang, S. Li, P. Xu, Recent advances in magnetic field-enhanced electrocatalysis, ACS Appl. Energy Mater. 3 (2020) 10303–10316.
- [12] T. Singh, T. Miyasaka, Stabilizing the efficiency beyond 20% with a mixed cation perovskite solar cell fabricated in ambient air under controlled humidity, Adv. Energy Mater. 8 (2018), 1700677.
- [13] Z. Yu, X. Yue, J. Fan, Q. Xiang, Crystalline intramolecular ternary carbon nitride homojunction for photocatalytic hydrogen evolution, ACS Catal. 12 (2022) 6345–6358.

[14] R. Du, W. Yi, W. Li, H. Yang, H. Bai, J. Li, G. Xi, Quasi-metal microwave route to MoN and Mo₂C ultrafine nanocrystalline hollow spheres as surface-enhanced raman scattering substrates, *ACS Nano* 14 (2020) 13718–13726.

[15] E. Contreras, R. Nixon, C. Litts, W. Zhang, F.M. Alcorn, P.K. Jain, Plasmon-assisted ammonia electrosynthesis, *J. Am. Chem. Soc.* 144 (2022) 10743–10751.

[16] W. Zhang, S. Wang, S.A. Yang, X.-H. Xia, Y.-G. Zhou, Plasmon of Au nanorods activates metal–organic frameworks for both the hydrogen evolution reaction and oxygen evolution reaction, *Nanoscale* 12 (2020) 17290–17297.

[17] X. Zeng, S.M. Choi, Y. Bai, M.J. Jang, R. Yu, H.-S. Cho, C.-H. Kim, N.V. Myung, Y. Yin, Plasmon-enhanced oxygen evolution catalyzed by Fe₂N-embedded TiO_xN_y nanoshells, *ACS Appl. Energy Mater.* 3 (2020) 146–151.

[18] L. Du, G. Shi, Y. Zhao, X. Chen, H. Sun, F. Liu, F. Cheng, W. Xie, Plasmon-promoted electrocatalytic water splitting on metal-semiconductor nanocomposites: the interfacial charge transfer and the real catalytic sites, *Chem. Sci.* 10 (2019) 9605–9612.

[19] G. Liu, P. Li, G. Zhao, X. Wang, J. Kong, H. Liu, H. Zhang, K. Chang, X. Meng, T. Kako, J. Ye, Promoting active species generation by plasmon-induced hot-electron excitation for efficient electrocatalytic oxygen evolution, *J. Am. Chem. Soc.* 138 (2016) 9128–9136.

[20] J. Xu, P. Gu, D.J.S. Birch, Y. Chen, Plasmon-promoted electrochemical oxygen evolution catalysis from gold decorated MnO₂ nanosheets under green light, *Adv. Funct. Mater.* 28 (2018), 1801573.

[21] T. Wu, S. Sun, J. Song, S. Xi, Y. Du, B. Chen, W.A. Sasangka, H. Liao, C.L. Gan, G. G. Scherer, L. Zeng, H. Wang, H. Li, A. Grimaud, Z.J. Xu, Iron-facilitated dynamic active-site generation on spinel CoAl₂O₄ with self-termination of surface reconstruction for water oxidation, *Nat. Catal.* 2 (2019) 763–772.

[22] Q. Zhang, Z. Yang, X. Chen, S. Ning, Y. Qi, L. Liu, J. Ye, Plasmon-enhanced CO selective oxidation in H₂ over Pt nanoclusters supported on metallic molybdenum dioxide nanocrystals, *Adv. Mater. Interfaces* 7 (2020), 2001657.

[23] Q. Zhang, X. Li, W. Yi, W. Li, H. Bai, J. Liu, G. Xi, Plasmonic MoO₂ nanospheres as a highly sensitive and stable non-noble metal substrate for multicomponent surface-enhanced Raman analysis, *Anal. Chem.* 89 (2017) 11765–11771.

[24] Q. Zhang, X. Li, Q. Ma, Q. Zhang, H. Bai, W. Yi, J. Liu, J. Han, G. Xi, A metallic molybdenum dioxide with high stability for surface enhanced Raman spectroscopy, *Nat. Commun.* 8 (2017) 14903.

[25] G. Xi, J. Ye, Q. Ma, N. Su, H. Bai, C. Wang, In situ growth of metal particles on 3D urchin-like WO₃ nanostructures, *J. Am. Chem. Soc.* 134 (2012) 6508–6511.

[26] Z. Kou, Y. Yu, X. Liu, X. Gao, L. Zheng, H. Zou, Y. Pang, Z. Wang, Z. Pan, J. He, S. J. Pennycook, J. Wang, Potential-dependent phase transition and Mo-enriched surface reconstruction of γ-CoOOH in a heterostructured Co-Mo₂C precatalyst enable water oxidation, *ACS Catal.* 10 (2020) 4411–4419.

[27] S. Kurth, J.P. Perdew, P. Blaha, Molecular and solid-state tests of density functional approximations: LSD, GGAs, and meta-GGAs, *Int. J. Quantum Chem.* 75 (1999) 889–909.

[28] R.O. Jones, O. Gunnarsson, The density functional formalism, its applications and prospects, *Rev. Mod. Phys.* 61 (1989) 689–746.

[29] J.K. Nørskov, J. Rossmeisl, A. Logadottir, L. Lindqvist, J.R. Kitchin, T. Bligaard, H. Jónsson, Origin of the overpotential for oxygen reduction at a fuel-cell cathode, *J. Phys. Chem. B* 108 (2004) 17886–17892.

[30] M. Otani, O. Sugino, First-principles calculations of charged surfaces and interfaces: a plane-wave nonrepeated slab approach, *Phys. Rev. B* 73 (2006), 115407.

[31] H. Chen, J. Chen, P. Ning, X. Chen, J. Liang, X. Yao, D. Chen, L. Qin, Y. Huang, Z. Wen, 2D heterostructure of amorphous CoFeB coating black phosphorus nanosheets with optimal oxygen intermediate absorption for improved electrocatalytic water oxidation, *ACS Nano* 15 (2021) 12418–12428.

[32] X. Chen, Z. Yu, L. Wei, Z. Zhou, S. Zhai, J. Chen, Y. Wang, Q. Huang, H.E. Karahan, X. Liao, Y. Chen, Ultrathin nickel boride nanosheets anchored on functionalized carbon nanotubes as bifunctional electrocatalysts for overall water splitting, *J. Mater. Chem. A* 7 (2019) 764–774.

[33] H. Chen, S. Ouyang, M. Zhao, Y. Li, J. Ye, Synergistic activity of Co and Fe in amorphous Cox-Fe-B catalyst for efficient oxygen evolution reaction, *ACS Appl. Mater. Interfaces* 9 (2017) 40333–40343.

[34] D. Guo, H. Chen, H. Tian, S. Ouyang, J. Wang, J. Lv, Modulation of an intermediate layer between NiCoP and Ni foam substrate in a microwire array electrode for enhancing the hydrogen-evolution reaction, *Chem. Commun.* 56 (2020) 4990–4993.

[35] S. Zhang, B. Huang, L. Wang, X. Zhang, H. Zhu, X. Zhu, J. Li, S. Guo, E. Wang, Boosted oxygen evolution reactivity via atomic iron doping in cobalt carbonate hydroxide hydrate, *ACS Appl. Mater. Interfaces* 12 (2020) 40220–40228.

[36] Y. Jin, H. Wang, J. Li, X. Yue, Y. Han, P.K. Shen, Y. Cui, Porous MoO₂ nanosheets as non-noble bifunctional electrocatalysts for overall water splitting, *Adv. Mater.* 28 (2016) 3785–3790.

[37] X. Li, Y. Wang, J. Wang, Y. Da, J. Zhang, L. Li, C. Zhong, Y. Deng, X. Han, W. Hu, Sequential electrodeposition of bifunctional catalytically active structures in MoO₃/Ni-NiO composite electrocatalysts for selective hydrogen and oxygen evolution, *Adv. Mater.* 32 (2020), 2003414.

[38] J.M.V. Nsanzimana, L. Gong, R. Dangol, V. Reddu, V. Jose, B.Y. Xia, Q. Yan, J.-M. Lee, X. Wang, Tailoring of metal boride morphology via anion for efficient water oxidation, *Adv. Energy Mater.* 9 (2019), 1901503.

[39] M.S. Burke, M.G. Kast, L. Trotocaud, A.M. Smith, S.W. Boettcher, Cobalt-iron (oxy)hydroxide oxygen evolution electrocatalysts: the role of structure and composition on activity, stability, and mechanism, *J. Am. Chem. Soc.* 137 (2015) 3638–3648.

[40] Y. Du, Z. He, F. Ma, Y. Jiang, J. Wan, G. Wu, Y. Liu, Anionic biopolymer assisted preparation of MoO₂@C heterostructure nanoparticles with oxygen vacancies for ambient electrocatalytic ammonia synthesis, *Inorg. Chem.* 60 (2021) 4116–4123.

[41] Y. Zhou, H. Xie, C. Wang, Q. He, Q. Liu, Z. Muhammad, Y.A. Haleem, Y. Sang, S. Chen, L. Song, Probing lithium storage mechanism of MoO₂ nanoflowers with rich oxygen-vacancy grown on graphene sheets, *J. Phys. Chem. C* 121 (2017) 15589–15596.

[42] E.S. Rountree, B.D. McCarthy, T.T. Eisenhart, J.L. Dempsey, Evaluation of homogeneous electrocatalysts by cyclic voltammetry, *Inorg. Chem.* 53 (2014) 9983–10002.

[43] H. Xu, C. Shan, X. Wu, M. Sun, B. Huang, Y. Tang, C.-H. Yan, Fabrication of layered double hydroxide microcapsules mediated by cerium doping in metal-organic frameworks for boosting water splitting, *Energy Environ. Sci.* 13 (2020) 2949–2956.

[44] H. Sun, C. Tian, G. Fan, J. Qi, Z. Liu, Z. Yan, F. Cheng, J. Chen, C.-P. Li, M. Du, Boosting activity on Co₃N porous nanosheet by coupling CeO₂ for efficient electrochemical overall water splitting at high current densities, *Adv. Funct. Mater.* 30 (2020), 1910596.

[45] Q. Wang, C.-Q. Xu, W. Liu, S.-F. Hung, H. Bin Yang, J. Gao, W. Cai, H.M. Chen, J. Li, B. Liu, Coordination engineering of iridium nanocluster bifunctional electrocatalyst for highly efficient and pH-universal overall water splitting, *Nat. Commun.* 11 (2020) 4246.

[46] C. Liu, J. Qian, Y. Ye, H. Zhou, C.-J. Sun, C. Sheehan, Z. Zhang, G. Wan, Y.-S. Liu, J. Guo, S. Li, H. Shin, S. Hwang, T.B. Gunnoe, W.A. Goddard, S. Zhang, Oxygen evolution reaction over catalytic single-site Co in a well-defined brookite TiO₂ nanorod surface, *Nat. Catal.* 4 (2021) 36–45.

[47] J.K. Nørskov, J. Rossmeisl, A. Logadottir, L. Lindqvist, J.R. Kitchin, T. Bligaard, H. Jónsson, Origin of the overpotential for oxygen reduction at a fuel-cell cathode, *J. Phys. Chem. B* 108 (2004) 17886–17892.

[48] J. Chen, Y. Chen, P. Li, Z. Wen, S. Chen, Energetic span as a rate-determining term for electrocatalytic volcanoes, *ACS Catal.* 8 (2018) 10590–11059.